

www.acsanm.org Article

Nanoscale Control of Intrinsic Magnetic Topological Insulator MnBi₂Te₄ Using Molecular Beam Epitaxy: Implications for Defect Control

Hyunsue Kim, Mengke Liu, Lisa Frammolino, Yanxing Li, Fan Zhang, Woojoo Lee, Chengye Dong, Yi-Fan Zhao, Guan-Yu Chen, Pin-Jui Hsu, Cui-Zu Chang, Joshua Robinson, Jiaqiang Yan, Xiaoqin Li, Allan H. MacDonald, and Chih-Kang Shih*



Cite This: ACS Appl. Nano Mater. 2024, 7, 21149-21159



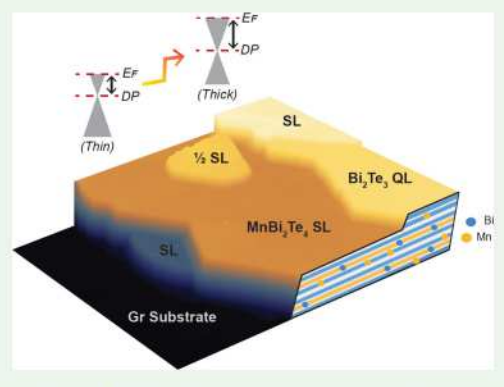
ACCESS

Metrics & More

Article Recommendations

s Supporting Information

ABSTRACT: Intrinsic magnetic topological insulators have emerged as a promising platform to study the interplay between the topological surface states and ferromagnetism. This unique interplay can give rise to a variety of exotic quantum phenomena, including the quantum anomalous Hall effect and axion insulating states. Here, utilizing molecular beam epitaxy (MBE), we present a comprehensive study of the growth of MnBi₂Te₄ thin films on Si (111), epitaxial graphene, and highly ordered pyrolytic graphite substrates. By combining a suite of in situ characterization techniques, we obtain critical insights into the nanoscale control of MnBi₂Te₄ epitaxial growth. First, we extract the free energy landscape for the epitaxial relationship as a function of the in-plane angular distribution. Then, by employing an optimized layer-by-layer growth, we determine the chemical potential and Dirac point of the thin film at different thicknesses and how this quantity is manifested by the dopant compensation from different antisite



defects. Overall, these results establish a foundation for understanding the growth kinetics of MnBi₂Te₄ and pave the way for future applications of MBE-grown thin films in emerging topological quantum materials.

KEYWORDS: magnetic topological insulator, MnBi2Te4 molecular beam epitaxy, electronic structure, antisite defect

■ INTRODUCTION

The emergence of magnetic topological insulators (MTIs) has created a promising material system to explore the interplay of magnetic and topological properties. 1-3 Specifically, MTI provides a rich playground to realize various topological states such as the axion insulator states and quantum anomalous Hall (QAH) states.4-7 Early attempts to realize these exotic quantum states primarily involved the addition of ferromagnetic dopants into otherwise nonmagnetic topological insulators (TIs), forming so-called extrinsic MTIs (eMTIs) [e.g., Cr-doped (Bi,Sb)₂Te₃].⁵⁻⁹ However, due to the spatial inhomogeneity of magnetic dopants, the realization of the QAH effect in eMTIs requires ultralow temperatures (30 mK). A significant recent development is the discovery of so-called intrinsic MTIs (iMTIs), which have enabled the realization of the QAH effect at a much higher temperature (~2 K). Such an improvement has led to a surge of interest in these materials. The family of Mn-Bi-Te compounds, e.g., MnBi₂Te₄ (MBT), has been the subject of extensive study as iMTIs. 9,10 Thus far, most investigations of MBT have been carried out using bulkgrown single crystals. 11-13 However, the bulk crystal is heavily degenerate n-type with the Fermi level $(E_{\rm F})$ located $\sim 0.25-0.3$ eV above the Dirac point (DP), which would obscure the

topological surface states due to hybridization with the bulk bands. Although successful device fabrications have been achieved on exfoliated single-crystal flakes, the method is not scalable. To overcome these limitations, developing epitaxial methods to grow iMTI thin films with precise control of thickness and effective tuning of electronic chemical potential is critical.

Molecular beam epitaxy (MBE) is a powerful technique that enables the precise control of layer thickness and dopant concentration in the growth of elemental and compound semiconductors. Therefore, the technique is expected to be adopted to grow thin films of MBT and its variants to provide a scalable material platform. Considering that it took several decades to refine the MBE growth of III—V compounds to achieve extremely precise control, we anticipate many challenges in the MBE growth of MTIs. 16,17 Nevertheless,

Received: August 6, 2024 Revised: August 20, 2024 Accepted: August 22, 2024 Published: August 28, 2024





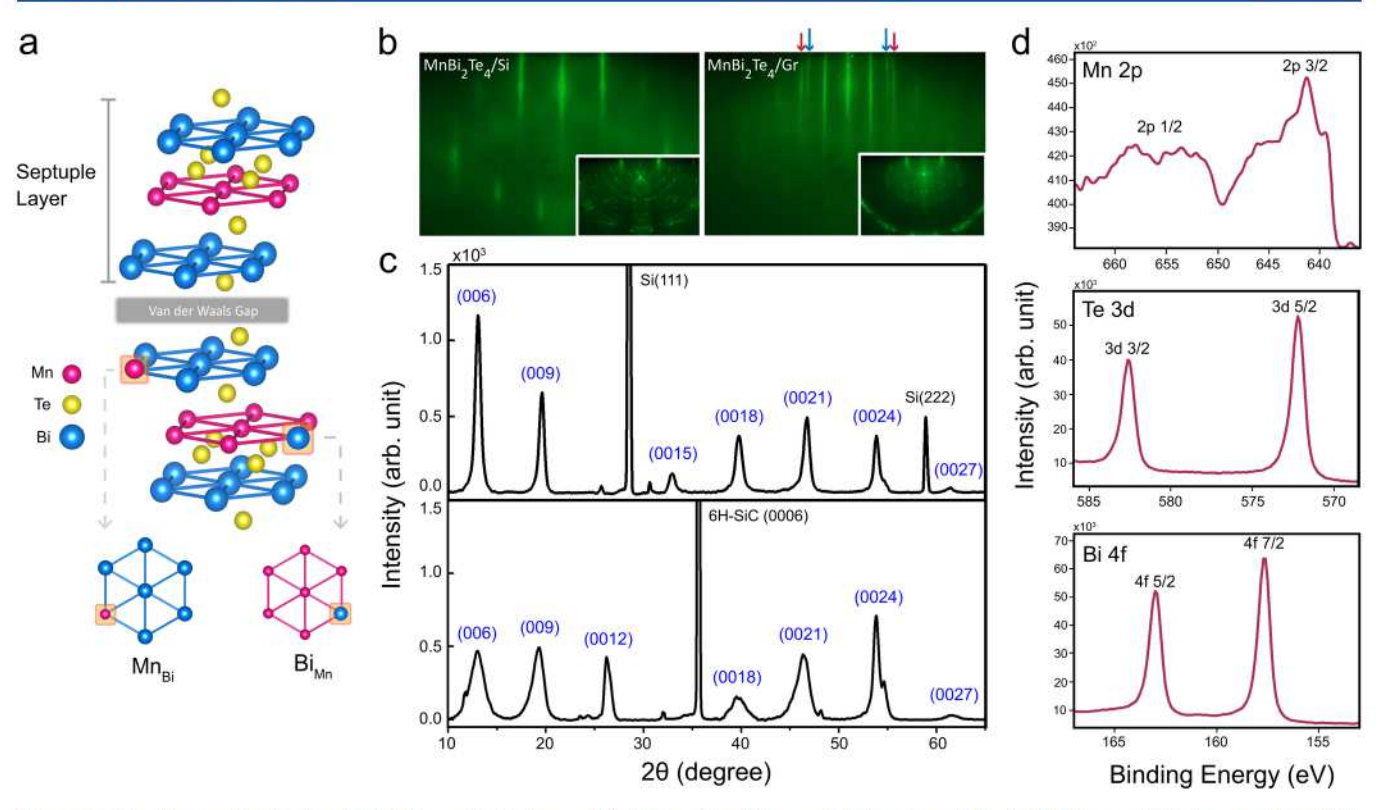


Figure 1. Crystal growth of a few $MnBi_2Te_4$ septuple layers. (a) Schematic of the crystal structure of the $MnBi_2Te_4$ septuple layer with antisite defects on Mn and Bi sites, which are common defects seen in MBE-grown samples. (b) RHEED images of an MBT/Si sample (left) and substrate (inset) and RHEED images of the MBT/BL-Gr sample (right) and substrate (inset). (c) Linear scale XRD measurement on MBT on Si (top) and BL-Gr (bottom), indicating both samples primarily consist of MBT (124). (d) XPS spectra on MBT/BL-Gr showing high-resolution Mn 2p, Bi 4f, and Te 3d spectra.

several groups have reported the MBE growth of MBT.^{18–26} In these previous studies, the main goal was to control the growth parameters to form Mn, Bi, and Te septuple layers (SL), Te—Bi—Te—Mn—Te—Bi—Te, with minimal defects.

In this work, by combining MBE growth with in situ characterization tools, we reveal several important insights into the nanoscale control of MBE growth in MBT thin films. We have chosen two different substrates, Si (111) and epitaxial bilayer graphene (BL-Gr) to explore the effect of lattice match and interfacial chemical bonding. Specifically, we empirically extract the free energy landscape for the epitaxial relationship as a function of in-plane lattice orientation through spot-profile analysis of low-energy electron diffractions. Such insight provides an important guideline for the refinement of epitaxial growth. Moreover, by using in situ scanning tunneling microscopy (STM), we investigate the surface structure of MBT/highly ordered pyrolytic graphite (HOPG) on the atomic scale and achieve layer-by-layer growth. By using scanning tunneling spectroscopy (STS) and angle-resolved photoelectron spectroscopy (ARPES), we investigate the evolution of the electronic chemical potential and the DP from which we extract the interplay of two key antisite defects: Mn_{Bi} as a p-type dopant and Bi_{Mn} as an n-type dopants. Our study provides essential insights into growth kinetics and defect control, establishing a foundation for the future development of MBE growth of iMTIs on various substrates and their heterostructures, which is influential for advancing thin-film device applications.

RESULTS AND DISCUSSION

Controlling Stoichiometry. Epitaxial MBT films are grown using MBE on a Si (111) 7 × 7 reconstruction surface and epitaxial BL-Gr/SiC substrates. These growths are established by the coevaporation of Mn, Bi, and Te with an additional post-annealing process under Te ambient. Since three chemical elements are deposited on the substrate simultaneously, the parameter window for the optimal substrate temperature for self-assembly is rather narrow. Also, the Te flux is kept excessive during growth to improve crystallinity and minimize defect formation. Further details on the growth parameters can be found in the Methods section. Figure 1a is a schematic showing the crystal structure of two septuple layers stacked with a van der Waals gap in between. Antisite defects between Mn and Bi (marked as Mn_{Bi} and Bi_{Mp}) are routinely seen in MBE-grown films.

The highly crystalline MBE-grown MBT films are confirmed by reflection high-energy electron diffraction (RHEED) patterns shown in Figure 1b on Si (left) and BL-Gr (right) substrates. The bright and sharp streaks on both patterns indicate that the sample is grown uniformly with high crystallinity on both substrates. Additional streaks marked with blue arrows in Figure 1b appear only on the MBT/BL-Gr RHEED patterns. The streaks indicate the coexistence of two different domains with 0° and 30° alignments to the substrate. Further analysis of the coexisting phases using low-energy electron diffraction (LEED) will be discussed later. Figure 1c shows θ –2 θ X-ray diffraction (XRD) scans of the MBT/Si (top) and MBT/BL-Gr (bottom) on a linear scale. The same scan is plotted on the log scale in Figure S1. Note that the

substrate signals at 25-30° for Si (111) and 31.4-37° for 6H-SiC (0006) are attenuated by a factor of 100 to prevent the substrate peak from overwhelming nearby peaks. Comparing the XRD spectra of MBT/Si and MBT/BL-Gr, the MBT film grown on the BL-Gr substrate has generally broader peaks than the film grown on the Si substrate throughout the scan. Focusing on the (009) peak, the peak width on the MBT/BL-Gr system is broader than the peak measured on the MBT/Si system by about a factor of 2. This feature is most likely due to the coexistence of the two domains orientated 30° to each other. Although the films predominantly consist of the MBT(124) phase, a trace of MnTe remains and appears at the shoulder of the (0024) peak. This suggests a partial contribution from other phases of MBT.¹⁸ A direct comparison of the XRD peaks with variations in the flux ratio and substrate temperatures is shown in Figure S2. Furthermore, core-level photoelectron spectroscopy was taken on the MBT/BL-Gr system with an Al K α source at $h\nu = 1486.6$ eV (Figure 1d), showing the expected Mn 2p, Bi 4f, and Te 3d peaks with minimal oxidation states thanks to the quasi in situ transfer between the MBE in ultrahigh vacuum (UHV) to a glovebox. The elemental ratio of Mn/Bi, extracted from Figure 1d, is 1:1.92. Comparable XPS spectra on MBT/Si and cleaved bulk MBT samples are measured under the same conditions, showing the high-resolution Mn 2p, Bi 4f, and Te 3d spectra (Figures S3 and S4).

Free Energy Landscape for In-Plane Orientational Alignments. For most epitaxially grown samples, the lattice matching condition of substrates to the sample plays a critical role. Among many candidate materials for substrates, listed in Table 1, Bi₂Te₃ (BT) or BaF₂ provides minimal lattice

Table 1. Substrate Lattice Matching Condition Compared to the MnBi₂Te₄ Lattice

system	$(A)^{a_{\mathrm{cubic}}}$	$a_{ m basal} \atop ({ m A})$	$^{a_{R30}}_{ m (A)}$	lattice match to MnBi ₂ Te ₄
MnBi ₂ Te ₄		4.33		1.00
Bi_2Te_3 (0001)		4.38		1.012
BaF ₂ (111)	6.20	4.38		1.012
GaAs (111)	5.65	4.00		0.923
Si (111)	5.43	3.84		0.887
STO (111)	3.91	2.76		(3:2) 0.956
Al ₂ O ₃ (0001)		4.79		1.105
graphene		2.46		(7:4) 0.994
70000			4.26	$(\sqrt{3})$ 0.984

mismatch (\sim 1.2%) with the MBT sample. Si (111), on the other hand, has a relatively large mismatch with MBT (~11.3%). Nevertheless, Si (111) is often used as a substrate. In Figure 2a, the LEED pattern of MBT grown on Si (111) 7 × 7 shows 6-fold symmetry, reflecting a good orientational alignment. The full width at half-maximum (FWHM) of the diffraction spots shows an angular dispersion of $\sigma_{\theta} = 11^{\circ}$, presumably due to a large lattice mismatch. The LEED pattern shows a 6-fold symmetry with nearly equal intensity for individual spots. Note, however, that the surface crystal structure of MBT breaks the inversion symmetry. This symmetry breaking should result in inequivalence in intensity between \vec{q} and $-\vec{q}$ where \vec{q} is the wave vector of the diffraction spot. In Figure 2b, we present the LEED pattern for a cleaved single crystal of MBT where such an asymmetry can be observed from the spot profile shown below. The nearly

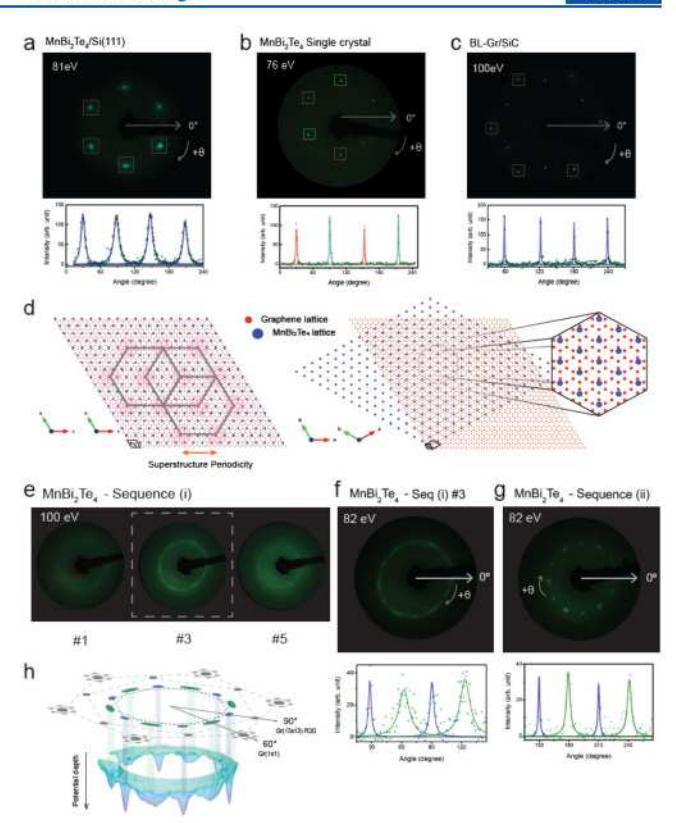


Figure 2. Evolution of the LEED patterns. (a-c) LEED patterns of MBT/Si at electron energy 81 eV, bulk MBT crystal measured at hv=76 eV, and bilayer graphene substrate measured at hv=100 eV, respectively. Corresponding radial intensity cut along the direction shown in the panel. The peaks with higher intensity are marked with green boxes, and those with lower intensity are marked with red boxes in panel b. (d) Superstructures between MBT (124) and epitaxial graphene substrate at 0° and 30° relative rotations. (e) LEED pattern after growth at RT and immediate annealing at 217 °C (#1), postanneal at 250 °C for 1 h (#3), and post-anneal at 300 °C for 1 h (#5). (f) Selected optimal annealing cycle (#3) measured at 82 eV for the radial cut. (g) Further improved growth of MBT deposited at RT and annealed at 257 °C with 0.35 Mn/Bi flux ratio. (h) A qualitative sketch of the potential energy landscape is obtained by inverting the LEED spot profile intensity as a function of the rotation angle.

symmetric spots for the MBE-grown MBT on Si (111) indicate that the surface contains nearly equal populations for the twin domains. The spot profile for the single crystal shows an angular dispersion of $\sigma_{\theta} = 2.0^{\circ}$. This value is slightly larger than the value of $\sigma_{\theta} = 1.2^{\circ}$ observed on epitaxial graphene (Figure 2c), which likely corresponds to the resolution limit of our instrument.

Furthermore, graphene as a van der Waals substrate (with hexagonal boron nitride as the insulating equivalent), provides an intriguing platform for electronic device fabrication. We propose a method for growing MBT films directly on such substrates. Because of the formation of different alignments between MBT and epitaxial graphene, controlling Mn incorporation can be particularly challenging. However, we demonstrated the ability to control domain concentration by adjusting the Mn and Bi flux ratio, highlighting the importance of stoichiometric control. The van der Waals interface between epitaxial BL-Gr and MBT offers an opportunity to investigate the competition between these two orientational alignments through a LEED pattern analysis. We conducted a comprehensive LEED spot profile analysis on samples grown

by using three different growth sequences. Sequence (i) entails the growth of MBT thin film on epitaxial graphene with a Mn/ Bi flux ratio of 0.59, while sequence (ii) pertains to the growth of MBT thin film on epitaxial graphene with a Mn/Bi flux ratio of 0.35. Additionally, sequence (iii), which involves the growth of Bi2Te3 thin film on epitaxial graphene, is discussed in detail in the Supporting Information. Each sequence starts with the deposition of the film at near room temperature, followed by successive post-annealing cycles with different annealing temperatures. The room temperature deposition leads to randomly distributed orientations. The post-growth annealing procedure then allows these individual grains to merge and reorient toward the free energy minima. Thus, the growth procedure used in LEED analysis is similar to solid-phase epitaxy (SPE). Note that the films are annealed under Te vapor pressure to prevent the loss of Te atoms from the film. Table 2 summarizes the deposition and annealing conditions in

Table 2. Growth and Annealing Parameters for MnBi₂Te₄ on Epitaxial Graphene and Bi₂Te₃ on Epitaxial Graphene for Investigating the Sample–Substrate Epitaxial Relationship

	1	growth parame	anne	anneal parameter		
MnBi ₂ Te ₄	temp (°C)	deposition time (min)	Mn/Bi flux ratio	temp (°C)	anneal time (min)	
#1 (sequence 1)	RT	30	0.59	217	60	
#2				217	120	
#3				250	60	
#4				273	60	
#5				300	60	
sequence 2	RT	45	0.35	257	60	
	gr	rowth paramete	anneal	anneal parameter		
Bi ₂ Te ₃	temp (°C)	deposition (min		temp (°C)	anneal time (min)	
#1 (sequence	RT	30		250	60	
#2				250	120	
#3				300	60	
#4				300	120	

each sequence. Based on the graphene lattice constant of 2.46 Å, Table 3 presents lattice match conditions for BT, MnTe,

Table 3. Lattice Mismatch between MBT, BT, MT and the Epitaxial Graphene Substrate

lattice match with a _{Gi}	hing condition , = 2.46 Å	$a_{\rm (M,B)T}/1.75a_{\rm gr}$	$a_{(M,B)T}/\sqrt{3}a_{g}$
a_{BT}	4.38 Å	1.017	1.028
a_{MT}	4.13 Å	0.959	0.969
a_{MBT}	4.33 Å	1.005	1.016

and MBT against the graphene substrate along the 1×1 orientation (0° alignment), featuring a 7:4 coincidental lattice match between MBT and graphene. Moreover, Figure 2d visualizes the alignment along the $\sqrt{3}\times\sqrt{3}$ R30° orientation (R30° alignment), highlighting a nearly 1:1 lattice match between MBT and graphene substrate.

Sequence (i) involves MBE-grown MBT film with a Mn/Bi flux ratio of 0.59, followed by multiple post-annealing cycles. After deposition at room temperature and immediate annealing at 217 °C for 1 hour, the domains remain randomly oriented, reflected by the nearly invisible diffraction pattern

(Figure 2e #1). Subsequent annealing at 250 °C for an hour results in the emergence of two major domains (#3) along 0° and 30° alignments. Figure 2f illustrates clearer diffraction patterns for cycle #3 measured at 82 eV. The 0° domains display an angular dispersion of $\sigma_{\theta} = 13^{\circ}$ while the R30°domains exhibit a much sharper angular dispersion of σ_{θ} = 3.7°. Additionally, the integrated intensity ratio between the R30° and the 0° domains is 0.31, indicating that the population of the R30° domains comprises about 30% of the 0° domains. Annealing at an even higher temperature of 300 °C leads to film decomposition (#5). The result of the annealing sequence enables us to determine an optimal annealing temperature range of 250-273 °C. The LEED images of the full sequence (including #2 and #4) are shown in Figure S5a. In sequence (i), we utilize a Mn/Bi flux ratio of 0.59 to ensure Mn incorporation and identify the behavior when the sample involves a substantial population of the MnTe phase. This phase possesses a nontrivial lattice mismatch along either the 0° or R30° (3-4%) domains (Table 3). The presence of this phase mixture is likely to impact the kinetics of the in-plane alignment.

Sequence (ii) is designed to address the impact of the Mn/Bi flux ratio. In this sequence, a flux ratio of 0.35 is used. Instead of interrupting the procedure and taking LEED sequentially, we immediately anneal the film after the room temperature deposition at the optimal condition of 257 °C (annealing temperature) for 1 h. The resulting LEED pattern, shown in Figure 2g, demonstrates dramatic improvement for both the R30° and 0° domains, exhibiting an apparent 12-fold rotation symmetry. The angular dispersion for the R30° alignment is remarkably sharp, with $\sigma_{\theta} = 2.6^{\circ}$, a value comparable to $\sigma_{\theta} =$ 2.0° for the single crystal. The angular dispersion for the 0° domain is also significantly enhanced, yielding a value of σ_{θ} = 4.5°. In contrast, Figure 2f displays $\sigma_{\theta} = 13.0^{\circ}$ for the 0° alignment (#3). This dramatic improvement in the rotational alignment for both domains suggests that flux optimization enhances the epitaxial alignment on the van der Waals substrate. Consequently, the R30°/0° domain population ratio is improved to 0.46. We attribute the increased relative population for the R30° domain is due to the residual lattice mismatch of 1.6% along the $\sqrt{3} \times \sqrt{3}$ R30° direction.

Based on the LEED study, one can construct a free energy landscape for the orientational alignment between MBT and epitaxial BL-Gr as shown in Figure 2h. Along the ±30°, ±90°, and ±150° directions, there is a sharp and deep local free energy minimum. On the other hand, along the $\pm 60^{\circ}$, $\pm 120^{\circ}$, and ±180° directions, the local free energy minimum is shallower but broader. As this experiment starts with the thin film being deposited at room temperature, followed by postannealing at 257 °C, one can assume that the initial nucleation sites have randomly distributed orientations. The subsequent annealing procedure drives them to local free energy minima. Therefore, our results suggest that although the local minima near 60° are shallower and broader and the local minima at 90° are deeper and narrower, the barrier between them prevents an effective reorientation to the sharp minimum. Furthermore, using even higher annealing temperatures (nearly 300 °C) will not help since it will lead to the decomposition of MBT. We note that MBT thin films grown on both monolayer (ML)-Gr and BL-Gr substrates exhibit similar orientational alignments (Figure S6). In this LEED study, including the spot profile analysis, nontrivial information is offered on the in-plane alignment and the population ratio of different domains.

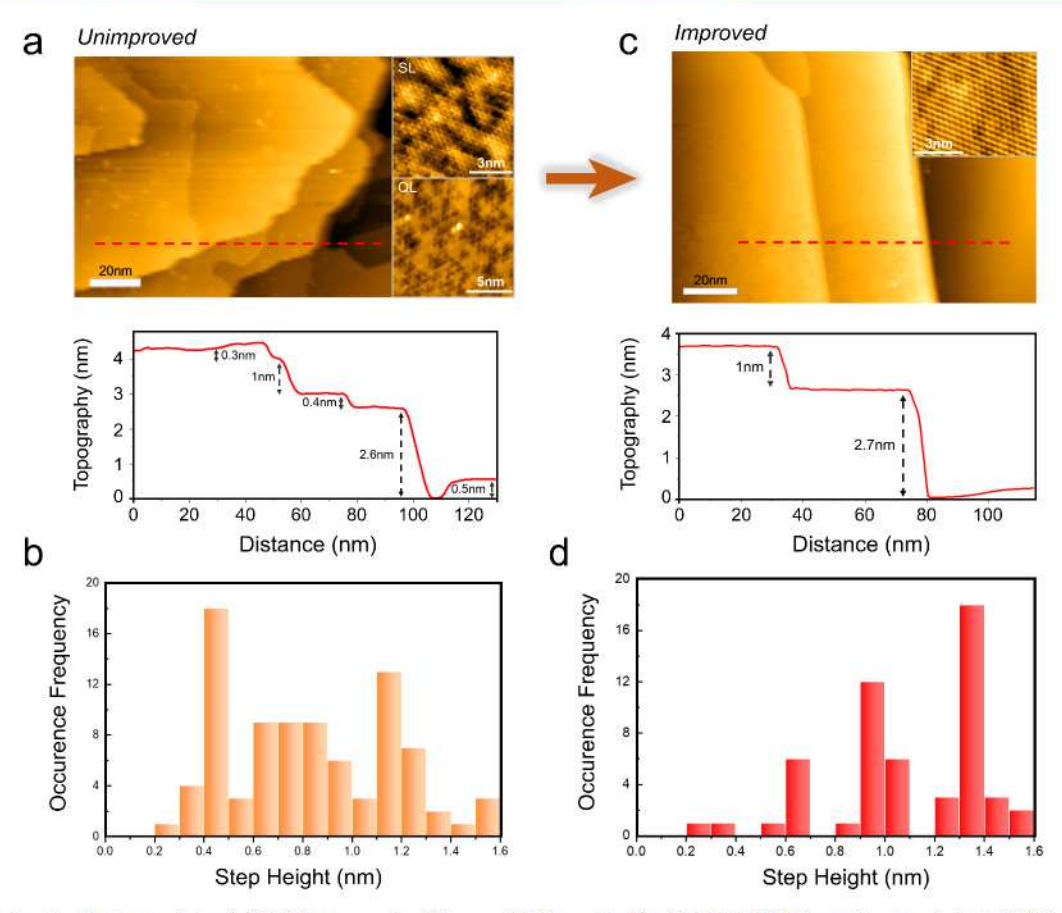


Figure 3. STM, fractional step analysis. (a) STM topography ($V_{\rm bias} = 4 \text{ V}$, $I_{\rm tun.} = 5 \text{ pA}$) of MBT/HOPG sample annealed at 200 °C. Corresponding profile cut entailing fractional step heights largely distributed around 0.3 and 0.7 nm. Atomic images of SL ($V_{\rm bias} = 1 \text{ V}$, $I_{\rm tun.} = 20 \text{ pA}$) and QL ($V_{\rm bias} = 1 \text{ V}$, $I_{\rm tun.} = 25 \text{ pA}$) terminated surfaces with signature defects. (b) Occurrence frequency of heights varying from 0.1 to 1.6 nm from sample scanned in panel a. (c) STM topography ($V_{\rm bias} = 2.5 \text{ V}$, $I_{\rm tun.} = 15 \text{ pA}$) of the MBT/HOPG sample annealed at 220 °C. Corresponding profile cutting through only containing mostly SL and QL. Inset represents SL termination atomic image ($V_{\rm bias} = -0.8 \text{ V}$, $I_{\rm tun.} = -25 \text{ pA}$). (d) Occurrence frequency of heights varying from 0.1 to 1.6 nm from panel c.

Through these three sequences, we have gained important understandings of how lattice match, the Mn/Bi flux ratio, and the growth/annealing temperature collaboratively influence the epitaxial quality of MnBi₂Te₄ on graphene.

Optimization of Layer-by-Layer Growth. The diffraction techniques (LEED, RHEED, and XRD) provide important information regarding crystallinity and crystal orientations. However, they do not provide microscopic information regarding the step height distributions or the distributions of various defects. For these specific observations, the *in situ* STM is a valuable tool for providing important insight.

Figure 3a shows the STM image of an unimproved MBT film with a nominal thickness of 5.8 SL grown at a substrate temperature of 200 °C. The surface contains multiple steps with various step heights, as seen in the line cut across the topography. The surface is mostly covered by fractional steps, and only a small portion of the surface contains terraces with a complete quintuple layer (QL \sim 1 nm) or septuple layer (SL \sim 1.35 nm) step height. Two inset atomic images in Figure 3a are acquired on the terraces of a SL step height (top) and a QL height (bottom). Interestingly, the STM images resemble those obtained on cleaved MnBi₄Te₇ single crystals where the surface termination entails both terraces of QL height and SL height. $^{27-29}$ On the QL terminated terrace, triangular dark defects, indicative of a MnBi antisite defect, are observed. Here,

a Mn atom replaces a Bi atom on the first sublayer, causing the three Te atoms to bond to it and appear in a dark depression. However, it is difficult to discern specific defects on the SL terminated terrace. One would observe complex defect structures with an inhomogeneous background, similar to those found on the SL terminated cleaved surface of MnBi₄Te₇. ²⁷⁻²⁹ This inhomogeneity reflects a mixture of defects in different sublayers, including Bi_{Mn} and Bi_{Te} antisite defects. Furthermore, the statistical distribution of step heights is extracted from an ensemble of many topography images (Figure 3b). The frequency distribution histogram shows a particularly large concentration of the following step heights: 0.3-0.4, 0.5-0.8, and 1.0-1.1 nm. 1.0-1.1 nm can seemingly be attributed to BT quintuple layers. However, fractional step heights, 0.3-0.4 and 0.5-0.8 nm, are likely formed due to the existence of uncombined MnTe layers as well as combinations of a few layers of MnTe, BT, and MBT, as illustrated by the cartoon images in Figure S7.

By iterating the growth parameters while utilizing the results of STM investigations for feedback, we achieved the growth of pristine MBT films at a substrate temperature of 220 °C. Figure 3c shows an example of the STM image of an improved film, where fractional steps are significantly minimized. The surface is left primarily with SL steps but with a minor presence of QL steps. Additional frequency distributions for the optimized sample are shown in Figure 3d. This residual QL

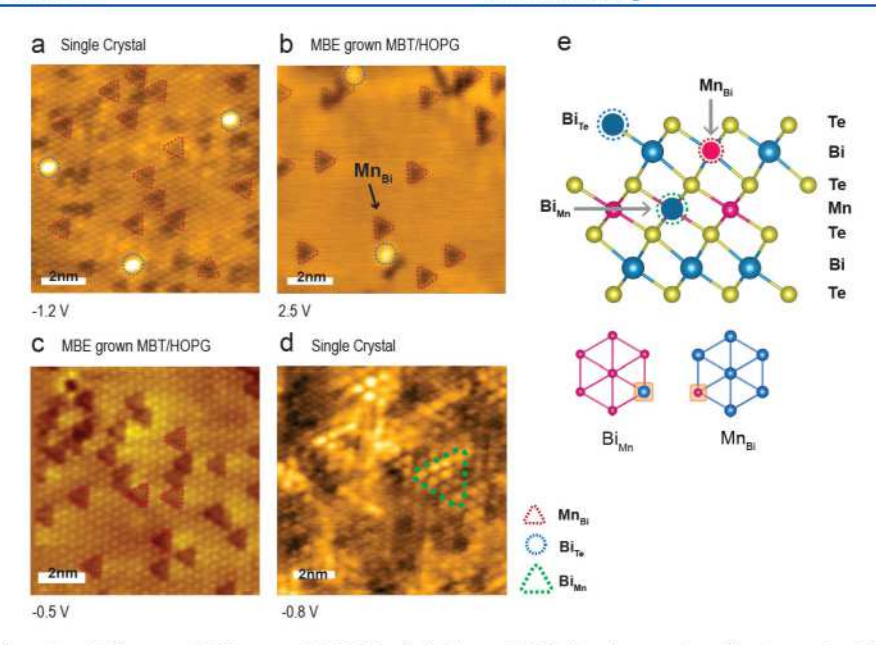


Figure 4. Identification of antisite defects on MBE-grown MnBi₂Te₄ (a) Cleaved MBT single crystal surface imaged at $V_{\rm bias} = -1.2$ V and $I_{\rm tun.} = 35$ pA, showing 35 Mn_{Bi} and 3 Bi_{Te}. MBE grown sample surface of MBT imaged at (b) $V_{\rm bias} = 2.5$ V, $I_{\rm tun.} = 20$ pA and (c) $V_{\rm bias} = -0.5$ V, $I_{\rm tun.} = -25$ pA in different regions. (d) STM topography of MBE grown MBT surface, imaged at $V_{\rm bias} = -0.8$ V and $I_{\rm tun.} = -35$ pA where Bi_{Mn} can be observed, marked with a green dashed triangle. (e) Schematics of septuple layer crystal structure indicating the location where Bi_{Mn} gets formed.

contribution indicates that the overall stoichiometry is still Mn deficient. The main difference between the samples includes a slightly elevated growth temperature by 20 °C as well as a post-growth annealing process under a 33% higher Te vapor background for 2/3 of the growth time (Figures 3a and 3c). Moreover, at the same Mn/Bi flux ratio, the resulting stoichiometry is subject to change when the substrate temperature is adjusted. The inset of Figure 3c shows a zoomed-in STM atomic image revealing the Te atomic lattice on the surface where low-density Mn_{Bi} antisite defects can be found.

Interplay of Defects and Electronic Structure. There are four types of antisite defects: (a) Mn_{Bi}, (b) Bi_{Mn}, (c) Bi_{Te}, and (d) TeBi. MnBi and BiTe are p-type dopants, while BiMn and TeBi are n-type dopants. As we discuss below, in our system, the dominant defects are Mn_{Bi} (p-type) and Bi_{Mn} (n-type). The formation energies of intrinsic defects, including these four antisite defects, as a function of the Fermi level (varied from the VBM to the CBM) in MnBi₂Te₄ and MnBi₄Te₇ under Te-rich or cation-rich conditions, has been calculated and reported.³⁰ The calculation shows that the formation energies of MnBi and BiMn, under the Te-rich condition (which corresponds to our growth condition), are significantly lower than those of other defects. Therefore, the MnBi and BiMn defects become more dominant. We first investigate the validity of this theoretical prediction. Identification and quantification of different point defects are important but also challenging tasks. For UHV-cleaved MnBi₂Te₄ single crystals, several groups have reported the observation of Bire, Mn_{Bi}, and Bi_{Mn} antisite defects using STM. 13,27-29 Figure 4a shows an STM image of a cleaved MnBi₂Te₄ surface. In this image, the Bi_{Te} antisite appears as a bright protrusion (marked by the blue dashed circles), while Mn_{Bi} appears as a dark trimer (marked by a dashed red triangle). In this 10 nm \times 10 nm image, one observes 3 Bi_{Te} (~0.5%) along with 35 \pm 5 Mn_{Bi} (~5.5%). In Figure 4b we show the same size STM image for an MBE-grown sample. Here, 2 Bi_{Te} (\sim 0.3%) and 18 \pm 2 Mn_{Bi}

(~3%) are observed. In another region, shown in Figure 4c of the MBE-grown sample, a higher number of MnBi antisite defects, containing 28 in a region 10 nm × 10 nm (corresponds to 4.5%), but no Bi_{Te} is observed. In this figure, one can observe the three depressed atomic sites associated with the three Te atoms that are bonded to the Mn underneath. We notice that the defect concentration is more homogeneous for bulk single crystal than that for the MBEgrown sample. The scarcer frequency for the observation of Bi_{Te} is consistent with a higher formation energy. Furthermore, we note that STM observation of TeBi has been reported for MBE-grown Bi₂Te₃ under Te-rich conditions.³¹ The Te_{Bi} antisite appears as a dark trimer (similar to MnBi), but to a larger spatial extent. The separation from the center of one dark spot to another dark spot in the trimer is due to two lattice constants for the TeBi. On the other hand, for MnBi, the separation is one lattice constant. During our investigation of the MBE-grown MBT sample, we never encountered any features indicating the TeBi antisite defect. We thus can rule out the interference of TeBi in our interpretation of dopant compensation. Thus, based on the calculation of formation energies and the STM visualization, we can safely conclude that the main defects in MBE-grown MBT film under Te-rich conditions would be Mn_{Bi} and Bi_{Mn} antisite defects.

Next, we discuss the Bi_{Mn} defect located at the Mn layer of the SL. Figure 4d shows an STM image (11 nm \times 11 nm), where one of the Bi_{Mn} is marked by the green dashed triangle. In this image, one can identify $\sim \! 10$ features that can be attributed to the Bi_{Mn} antisite defects, corresponding to only 1.5% concentration. However, it would be naive to assume that all Bi_{Mn} defects in the central layer are identifiable in the same manner. The main obstacle is that only those Bi_{Mn} point defects without other defects in the neighboring area can be identified this way. An isolated Bi_{Mn} antisite defect can influence a more extended region of the surface Te atoms. It has previously been reported that a Bi_{Mn} defect will result in a triangular protrusion, with 4 Te atoms on each side (namely, it

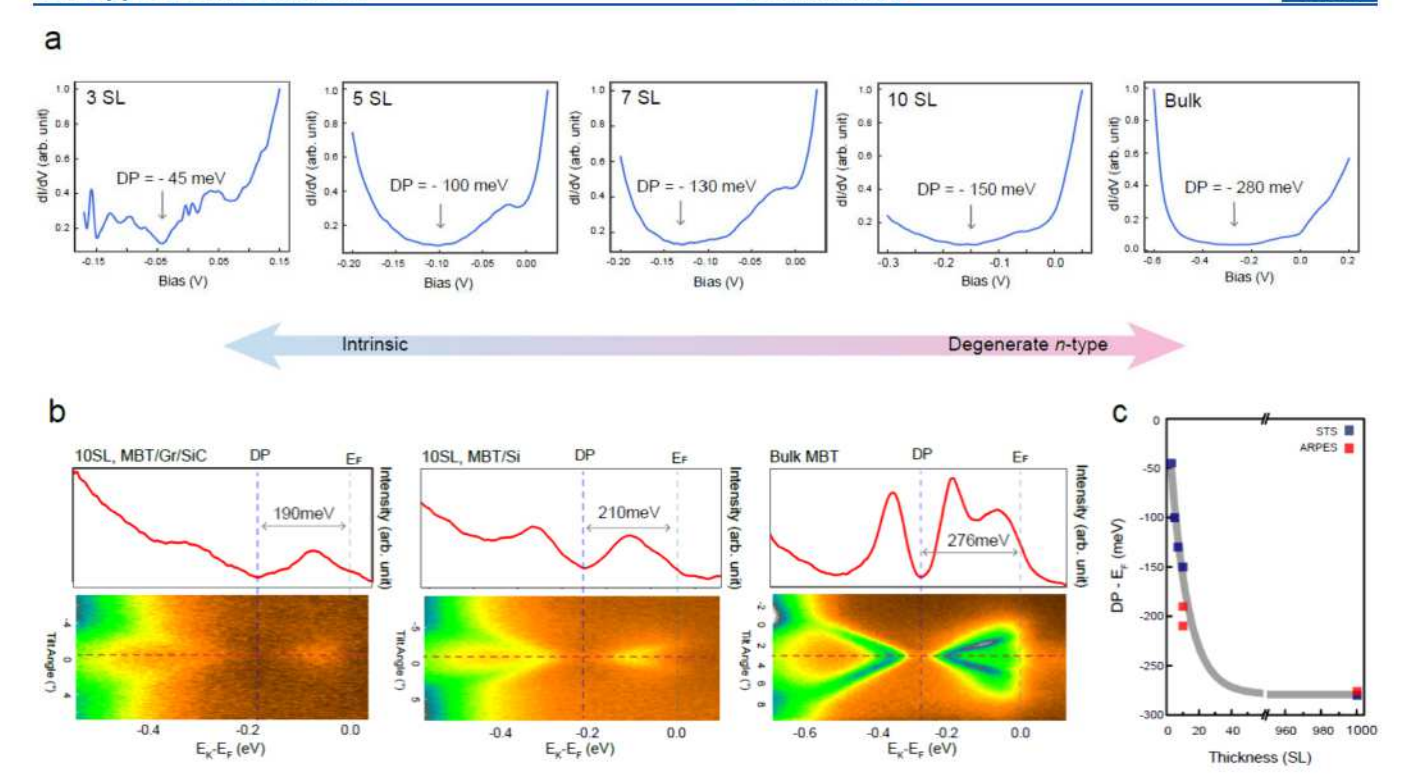


Figure 5. Thickness and defect concentration dependent DP evolution relative to $E_{\rm F}$. (a) Shift in Dirac point relative to $E_{\rm F}$ can be observed in dI/dV spectra on 3, 5, 7, 10 SL MBT/HOPG, and bulk MBT single crystal (represented as 1000 SL for curve fitting). (b) ARPES spectra on 10 SL MBT/BL-Gr, 10 SL MBT/Si, and bulk MBT. (c) A plot of DP- $E_{\rm F}$ extracted from STS as a function of thickness. The curve is plotted by fitting STS data (blue squares). DP reading from the ARPES data set (red squares) overlays the fitting curve.

impacts 10 Te atoms on the surface). Figure 4e illustrates the Bi_{Mn} defect embedded at the central layer of the SL, along with the positions of other antisite defects. Considering that we have, on average, 5% of Mn_{Bi} antisite defects in each bismuth sublattice and there are two bismuth layers in each SL, it requires over 10% of Bi_{Mn} antisite defects in the center Mn layer to make the sample degenerate n-type. If we use only the identifiable Bi_{Mn} antisite features in the STM image, we will grossly underestimate the concentration of Bi_{Mn} antisite defects. Thus, we believe that by using the Fermi level location relative to the Dirac point and the measured Mn_{Bi} concentration, we will obtain a better estimate of the Bi_{Mn} antisite concentration.

Evolution of Dirac Point and Fermi Energy. In an ideal MnBi₂Te₄, the exchange interaction of the topological surface states and the magnetic order leads to the formation of a Dirac mass gap that underpins the novel quantum transport properties such as QAHE. However, unambiguous experimental observation of the Dirac mass gap has been challenging. High-resolution, low-temperature ARPES measurements on cleaved MBT single crystals have yielded rather controversial results.^{32–34} Conversely, STS measurements on cleaved MBT single crystals consistently report the absence of a Dirac mass gap. However, interpretations regarding the reasons for this absence vary significantly. 13,29 Therefore, the ability to grow nearly intrinsic MBT films offers an excellent opportunity to tackle this issue. Our recent study has shown the interplay of magnetic defects and the formation of the Dirac mass gap by using the ultrathin regime (5 SL or less).35 The central discovery of this work leverages the observed lateral inhomogeneity in the MBT film, where defect densities vary from 2.5% to 9% across different probing regions. The low defect density (<4% Mn_{Bi} antisite) exhibits a clear Dirac mass

gap at a low temperature (4 K), which then vanishes at 77 K. On the other hand, when the Mn_{Bi} antisite defect density is large, the gap also vanishes below Neel temperature. These findings have been reported in ref 35 and will not be repeated berg.

As the Dirac mass gap disappears, we find that the Dirac point is located at ~ 50 meV below the Fermi level ($E_{\rm F}$) in the ultrathin regime. This indicates that the population of the ptype dopant, MnBi, is nearly compensated by that of the n-type dopant, Bi_{Mn}. 30 Observation of the antisite defects using an STM on the surface is relatively straightforward. However, individual Bi_{Mn} antisite defects can impact an array of surface Te atoms extended across many lattice sites. Hence, quantifying the local defect concentration is nontrivial due to the interference of multiple defects. Therefore, the energy difference between EF and the DP may serve as a better indicator for the density of the Bi_{Mn} antisite defects. As the MBT/HOPG film thickness increases, we find that the sample becomes progressively more n-type, as observed in Figure 5a. At a thickness of 10 SL, the energy difference between E_F and DP reaches ~150 meV, entering the degenerate n-type regime. As a comparison, we show STS measurement of the UHV cleaved bulk crystal of MBT, where the DP is found to be \sim 280 meV below the $E_{\rm F}$ value (Figure 5a).

In addition to STS studies, we also used ARPES to investigate the electronic structures of MBE films. Shown in Figure 5b are the ARPES spectra of several MBT films (nominally 10 SLs) grown on epitaxial BL-Gr and Si (111) substrates, respectively. These spectra are acquired at room temperature with hv = 21.2 eV. It has been shown previously that at hv = 21.2 eV, states near the DP are difficult to resolve, and the spectra always exhibit an apparent gap even when the

Table 4. Growth and Annealing Parameters for MnBi₂Te₄ on HOPG for the "Bad Growth" (Unimproved) and "Good Growth" (Improved) for STM Study as Well as MnBi₂Te₄ on Bilayer Graphene and Si (111) for ARPES Measurement

	$T_{\text{substrate}}$ $(^{\circ}\text{C})$	Mn source		Bi source			Te source			
		T _{Mn} (°C)	flux (Å/ 5 min)	T _{Bi} (°C)	flux (A/ 5 min)	Mn/Bi flux ratio	T _{Te} (°C)	flux (A/ 5 min)	$\frac{\Delta t_{ m g}}{({ m min})}$	$\Delta t_{\rm a} \ ({ m min})$
MBT/HOPG (unimproved)	200	283	1.42	525	2.90	0.49	223	11.39	45	30
MBT/HOPG (improved)	220	282	1.18	520	2.46	0.48	228	15.05	30	20
MBT/BLGr/SiC MBT/Si(111)	239 255	279 277	0.99 0.88	525 525	2.90 2.90	0.34	227 224	14.23 12.04	120 120	80 80

surface is gapless.³² Nevertheless, the DP location can still be inferred from the ARPES spectra and roughly coincides with the minimum of the energy dispersion curve (EDC) at the Γ point. The ARPES results for the 10 SL MBT film grown on epitaxial BL-Gr show a DP at -190 meV (relative to $E_{\rm F}$) (Figure 5b), indicating that the sample at this thickness is also degenerate n-type. The result is close to the STS result of -150 meV acquired on a nominal 10 SL film. We also note the spectrum exhibits a lower signal-to-noise ratio in comparison to the APRES data acquired on MBT film grown on Si (111) surface. This is likely the result of the existence of two domains for MBT films grown on BL-Gr, and one of them contains a large in-plane angular distribution. Nevertheless, as the E vs knear the Γ point is nearly isotropic, identification of the DP relative to the $E_{\rm F}$ is still possible. However, note that the apparent DP position is a macroscopic average, and there could be a large fluctuation in the DP position for individual grains. Moreover, in this thickness regime, quantifying thickness directly using STM is not feasible due to the loss of reference substrate in the image (Figure S8). Thus, the quoted thickness is estimated from the growth parameters. For a similar thickness of MBT film grown on Si (111) surfaces, the DP is located at -210 meV relative to E_F , also in the degenerate n-type regime. In comparison, the ARPES measurement of a UHV-cleaved MBT surface shows a heavily degenerate n-type surface with the DP at -280 meV relative to that of $E_{\rm F}$.

The combined STS and ARPES studies of MBE-grown MBT films on both Si (111) and epitaxial BL-Gr substrates indicate that for thick films with thickness greater than 10 SLs, the sample is degenerate n-type, similar to the case for the bulk MBT crystal. These results indicate that thick MBT films host large concentrations of Bi_{Mn} antisite defects, which is consistent with their bulk counterparts. The evolution of the DP-E_F as a function of thickness based on the STS measurement is plotted in Figure 5c. As one can see, in an ultrathin regime, the E_F is close to DP, suggesting that the ntype and p-type dopants are nearly compensated. On the other hand, as the film thickness increases, the sample rapidly approaches degenerate n-type, indicating that the n-type dopants (Bi_{Mn} antisite) far exceed the p-type dopant (Mn_{Bi}) concentration. Note that below 5 SL, one can find the local region that exposes the substrate, enabling a more precise determination of the local film thickness. Above 10 SL, the surface is fully covered with the MBT film with a typical 2-3 SL fluctuation. As the STS is measured in a local region, one needs to be aware that there is an uncertainty in thickness of

The evolution of the DP relative to $E_{\rm F}$ as a function of film thickness highlights the interesting interplay between n-type ${\rm Bi}_{\rm Mn}$ and p-type ${\rm Mn}_{\rm Bi}$ dopants. The progressively more n-type

characters with an increase in film thickness indicate that the concentration of Bi_{Mn} defects is more than that is required to compensate for the p-type MnBi dopants. From this behavior, entropically mixing Mn in the Bi layer and vice versa is expected. Why does the concentration of Bi_{Mn} defects positively correlate with the thickness? Previous reports have suggested that there exists a thermodynamic driving force toward the formation of high concentrations of Bi_{Mn} antisites defects. 30,36 Since MnTe has a smaller lattice constant relative to that of BT, the formation of Bi_{Mn} antisite defects can partially reduce the microscopic strain built up in the central Mn layer, forming an ideal Te-Bi-Te-Mn-Te-Bi-Te septuple layer. This thermodynamic driving force makes it difficult to avoid degenerate n-type doping in bulk MBT. However, such a microscopic strain is likely to be accommodated better in the ultrathin regime. Moreover, MBE growth is not a thermodynamic equilibrium process (in comparison to bulk crystal growth). Both effects may play important roles in causing nearly fully compensated doping in the ultrathin regime. Such a conjecture could be tested in future studies and could provide a strategy to grow electronically homogeneous films over a macroscopic length

■ CONCLUSIONS

In summary, we have investigated the MBE growth of MBT thin films on Si (111), BL-Gr, and HOPG substrates. The MBE growth is coupled with various in situ surface characterization techniques to gain insight into the atomistic mechanism underlying the growth. By using spot profile analysis of the LEED patterns, we map the free energy landscape for the in-plane orientational alignment between the epitaxial film and the substrate. In situ STM investigations allow us to observe the film topography and defect formations. These atomic details provide timely feedback that we use to optimize the growth parameters for high-quality thin films. STS and ARPES are employed to investigate the evolution of electronic chemical potential as a function of thickness, from which we gain insight into the interplay between the p-type Mn_{Bi} antisite defects and the n-type Bi_{Mn} antisite defects. In thin-film device fabrication, factors such as defect concentration, defect types, and domain boundaries significantly impact the performance. Our discussion explores these aspects in detail, proposing growth strategies that could be critical to enhancing device performance, primarily using surfacesensitive techniques. Our results provide a pathway to investigate material characteristics and deepen the understanding of the underlying growth mechanisms. Moreover, this approach extends beyond MBT, offering valuable insights into the engineering of other trielemental thin films.

MATERIALS AND METHODS

MBE Growth of MnBi $_2$ Te $_4$ Films. MnBi $_2$ Te $_4$ thin films were grown in a home-built MBE chamber with a base pressure of $\sim 10^{-10}$ Torr. Highly ordered pyrolytic graphite (HOPG) and bilayer epitaxial graphene substrates were outgassed at ~ 300 °C for 6 h before the growth. Si (111) substrate was prepared with the standard procedure of flashing via direct current heating up to ~ 1200 °C for an atomically clean surface with a well-defined 7 × 7 reconstruction. High-purity Mn (99.99%), Bi (99.999%), and Te (99.999%) were coevaporated from standard Knudsen cells. Samples studied with ARPES are grown at 240 °C (on graphene) and 255 °C (on Si) and post-annealed at the growth temperature in an excess Te ambient. Samples studied with LEED and RHEED were deposited at room temperature and postannealed in an excess ambient Te. Detailed growth parameters for the STM study are described in Table 4.

In Situ STM/STS and ARPES Measurements. Using a homebuilt UHV transfer system with base pressure $\sim 10^{-10}$ Torr to maintain the cleanness of the film, samples were transferred from the MBE chamber to STM (base pressure $\sim 10^{-11}$ Torr) and ARPES (base pressure $\sim 10^{-11}$ Torr) chambers without any exposure to air. STM/S measurements were conducted at 4.3 and 77 K. The W tip was prepared by electrochemical etching and cleaned by in situ electron-beam heating. STS dI/dV spectra were measured using a standard lock-in technique with feedback off, whose modulation frequency is 490 Hz. The ARPES measurements were carried out using a helium lamp with a beam spot diameter of $\sim 300~\mu m$ using a Scienta R3000 electron energy analyzer. The measurements were done with He I ($\sim 21.2~eV$) at room temperature.

ASSOCIATED CONTENT

Supporting Information

The Supporting Information is available free of charge at https://pubs.acs.org/doi/10.1021/acsanm.4c04518.

Additional X-ray diffraction measurement data, X-ray photoelectron spectroscopy measurement data, electron diffraction measurement data, morphology scan, and step height survey (PDF)

AUTHOR INFORMATION

Corresponding Author

Chih-Kang Shih — Department of Physics, The University of Texas at Austin, Austin, Texas 78712, United States;
o orcid.org/0000-0003-2734-7023; Email: shih@physics.utexas.edu

Authors

Hyunsue Kim – Department of Physics, The University of Texas at Austin, Austin, Texas 78712, United States

Mengke Liu — Department of Physics, The University of Texas at Austin, Austin, Texas 78712, United States

Lisa Frammolino – Department of Physics, The University of Texas at Austin, Austin, Texas 78712, United States

Yanxing Li — Department of Physics, The University of Texas at Austin, Austin, Texas 78712, United States

Fan Zhang – Department of Physics, The University of Texas at Austin, Austin, Texas 78712, United States

Woojoo Lee - Department of Physics, The University of Texas at Austin, Austin, Texas 78712, United States

Chengye Dong – 2D Crystal Consortium, The Pennsylvania State University, University Park, Pennsylvania 16802, United States

Yi-Fan Zhao — Department of Physics, The Pennsylvania State University, University Park, Pennsylvania 16802, United States Guan-Yu Chen – Department of Physics, National Tsing Hua University, 300044 Hsinchu, Taiwan

Pin-Jui Hsu — Department of Physics, National Tsing Hua University, 300044 Hsinchu, Taiwan; orcid.org/0000-0002-5704-6574

Cui-Zu Chang – Department of Physics, The Pennsylvania State University, University Park, Pennsylvania 16802, United States; © orcid.org/0000-0003-3515-2955

Joshua Robinson — 2D Crystal Consortium and Department of Physics, The Pennsylvania State University, University Park, Pennsylvania 16802, United States; ⊚ orcid.org/ 0000-0002-1513-7187

Jiaqiang Yan — Materials Science and Technology Division, Oak Ridge National Laboratory, Oak Ridge, Tennessee 37831, United States; oorcid.org/0000-0001-6625-4706

Xiaoqin Li — Department of Physics, The University of Texas at Austin, Austin, Texas 78712, United States; orcid.org/0000-0002-2279-3078

Allan H. MacDonald – Department of Physics, The University of Texas at Austin, Austin, Texas 78712, United States

Complete contact information is available at: https://pubs.acs.org/10.1021/acsanm.4c04518

Notes

The authors declare no competing financial interest.

ACKNOWLEDGMENTS

This work was primarily supported by the NSF through the Center for Dynamics and Control of Materials: an NSF Materials Research Science and Engineering Center under cooperative agreement no. DMR-1720595 and the US Air Force grant no. FA2386-21-1-4061. Other support is from the Air Force Office of Scientific Research grant no. FA2386-21-1-4067. Work done in Penn State is supported by 2DCC-MIP under NSF cooperative agreement DMR-1539916, DMR-2039351, ARO Award (W911NF2210159), as well as the support from Gordon and Betty Moore Foundation's EPiQS Initiative (GBMF9063 to C.-Z.C.). Work at Oak Ridge National Laboratory was supported by the US Department of Energy, Office of Science, Basic Energy Sciences, Materials Sciences and Engineering Division. P.J.H. acknowledges support from the National Science and Technology Council of Taiwan under grant no. NSTC-112-2636-M-007-006 and grant no. NSTC-110-2124-M-A49-008-MY3.

REFERENCES

(1) Li, R.; Wang, J.; Qi, X.-L.; Zhang, S.-C. Dynamical Axion Field in Topological Magnetic Insulators. *Nat. Phys.* 2010, 6 (4), 284–288.

(2) Mong, R. S. K.; Essin, A. M.; Moore, J. E. Antiferromagnetic Topological Insulators. *Phys. Rev. B* 2010, 81 (24), 245209.

(3) Tokura, Y.; Yasuda, K.; Tsukazaki, A. Magnetic Topological Insulators. Nat. Rev. Phys. 2019, 1 (2), 126-143.

(4) Mogi, M.; Kawamura, M.; Yoshimi, R.; Tsukazaki, A.; Kozuka, Y.; Shirakawa, N.; Takahashi, K. S.; Kawasaki, M.; Tokura, Y. A Magnetic Heterostructure of Topological Insulators as a Candidate for an Axion Insulator. *Nat. Mater.* 2017, 16 (5), 516–521.

(5) Yu, R.; Zhang, W.; Zhang, H.-J.; Zhang, S.-C.; Dai, X.; Fang, Z. Quantized Anomalous Hall Effect in Magnetic Topological Insulators. *Science* 2010, 329 (5987), 61–64.

(6) Chang, C.-Z.; Zhang, J.; Feng, X.; Shen, J.; Zhang, Z.; Guo, M.; Li, K.; Ou, Y.; Wei, P.; Wang, L.-L.; Ji, Z.-Q.; Feng, Y.; Ji, S.; Chen, X.; Jia, J.; Dai, X.; Fang, Z.; Zhang, S.-C.; He, K.; Wang, Y.; Lu, L.; Ma, X.-C.; Xue, Q.-K. Experimental Observation of the Quantum

- Anomalous Hall Effect in a Magnetic Topological Insulator. Science 2013, 340 (6129), 167-170.
- (7) Chang, C.-Z.; Zhao, W.; Kim, D. Y.; Zhang, H.; Assaf, B. A.; Heiman, D.; Zhang, S.-C.; Liu, C.; Chan, M. H. W.; Moodera, J. S. High-Precision Realization of Robust Quantum Anomalous Hall State in a Hard Ferromagnetic Topological Insulator. *Nat. Mater.* 2015, 14 (5), 473–477.
- (8) Dyck, J. S.; Hájek, P.; Lošťák, P.; Uher, C. Diluted Magnetic Semiconductors Based on Sb 2-x V x Te 3 (0.01 $\tilde{<}$ x < \sim 0.03). Phys. Rev. B 2002, 65 (11), No. 115212.
- (9) Otrokov, M. M.; Klimovskikh, I. I.; Bentmann, H.; Estyunin, D.; Zeugner, A.; Aliev, Z. S.; Gaß, S.; Wolter, A. U. B.; Koroleva, A. V.; Shikin, A. M.; Blanco-Rey, M.; Hoffmann, M.; Rusinov, I. P.; Vyazovskaya, A. Y.; Eremeev, S. V.; Koroteev, Y. M.; Kuznetsov, V. M.; Freyse, F.; Sánchez-Barriga, J.; Amiraslanov, I. R.; Babanly, M. B.; Mamedov, N. T.; Abdullayev, N. A.; Zverev, V. N.; Alfonsov, A.; Kataev, V.; Büchner, B.; Schwier, E. F.; Kumar, S.; Kimura, A.; Petaccia, L.; Di Santo, G.; Vidal, R. C.; Schatz, S.; Kißner, K.; Ünzelmann, M.; Min, C. H.; Moser, S.; Peixoto, T. R. F.; Reinert, F.; Ernst, A.; Echenique, P. M.; Isaeva, A.; Chulkov, E. V. Prediction and Observation of an Antiferromagnetic Topological Insulator. *Nature* 2019, 576 (7787), 416–422.
- (10) Deng, Y.; Yu, Y.; Shi, M. Z.; Guo, Z.; Xu, Z.; Wang, J.; Chen, X. H.; Zhang, Y. Quantum Anomalous Hall Effect in Intrinsic Magnetic Topological Insulator MnBi2Te4. *Science* 2020, 367 (6480), 895–900
- (11) Yan, J.-Q.; Zhang, Q.; Heitmann, T.; Huang, Z.; Chen, K. Y.; Cheng, J.-G.; Wu, W.; Vaknin, D.; Sales, B. C.; McQueeney, R. J. Crystal Growth and Magnetic Structure of MnBi 2 Te 4. *Phys. Rev. Mater.* 2019, 3 (6), No. 064202.
- (12) Li, H.; Liu, S.; Liu, C.; Zhang, J.; Xu, Y.; Yu, R.; Wu, Y.; Zhang, Y.; Fan, S. Antiferromagnetic Topological Insulator MnBi2Te4: Synthesis and Magnetic Properties. *Phys. Chem. Chem. Phys.* 2020, 22 (2), 556–563.
- (13) Yuan, Y.; Wang, X.; Li, H.; Li, J.; Ji, Y.; Hao, Z.; Wu, Y.; He, K.; Wang, Y.; Xu, Y.; Duan, W.; Li, W.; Xue, Q.-K. Electronic States and Magnetic Response of MnBi ₂ Te ₄ by Scanning Tunneling Microscopy and Spectroscopy. *Nano Lett.* 2020, 20 (5), 3271–3277.
- (14) Ploog, K. Delta- (°-) Doping in MBE-Grown GaAs: Concept and Device Application. J. Cryst. Growth 1987, 81 (1-4), 304-313.
- (15) Pessa, M.; Asonen, H.; Varrio, J.; Salokatve, A. A Comparative Study of Molecular Beam Epitaxy Methods. *Phys. Status Solidi A* 1989, 116 (2), 443–455.
- (16) Tsaur, B.; Metze, G. M. Molecular Beam Epitaxy of GaAs and AlGaAs on Si. Appl. Phys. Lett. 1984, 45 (5), 535-536.
- (17) Ballestad, A.; Ruck, B. J.; Schmid, J. H.; Adamcyk, M.; Nodwell, E.; Nicoll, C.; Tiedje, T. Surface Morphology of GaAs during Molecular Beam Epitaxy Growth: Comparison of Experimental Data with Simulations Based on Continuum Growth Equations. *Phys. Rev. B* 2002, 65 (20), No. 205302.
- (18) Liu, N.; Schreyeck, S.; Fijalkowski, K. M.; Kamp, M.; Brunner, K.; Gould, C.; Molenkamp, L. W. Antiferromagnetic Order in MnBi2Te4 Films Grown on Si(1 1 1) by Molecular Beam Epitaxy. *J. Cryst. Growth* 2022, 591, No. 126677.
- (19) Gong, Y.; Guo, J.; Li, J.; Zhu, K.; Liao, M.; Liu, X.; Zhang, Q.; Gu, L.; Tang, L.; Feng, X.; Zhang, D.; Li, W.; Song, C.; Wang, L.; Yu, P.; Chen, X.; Wang, Y.; Yao, H.; Duan, W.; Xu, Y.; Zhang, S.-C.; Ma, X.; Xue, Q.-K.; He, K. Experimental Realization of an Intrinsic Magnetic Topological Insulator. *Chin. Phys. Lett.* 2019, 36 (7), No. 076801.
- (20) Zhu, K.; Bai, Y.; Hong, X.; Geng, Z.; Jiang, Y.; Liu, R.; Li, Y.; Shi, M.; Wang, L.; Li, W.; Xue, Q.-K.; Feng, X.; He, K. Investigating and Manipulating the Molecular Beam Epitaxy Growth Kinetics of Intrinsic Magnetic Topological Insulator MnBi ₂ Te ₄ with *in Situ* Angle-Resolved Photoemission Spectroscopy. *J. Phys.: Condens. Matter* 2020, 32 (47), 475002.
- (21) Lapano, J.; Nuckols, L.; Mazza, A. R.; Pai, Y.-Y.; Zhang, J.; Lawrie, B.; Moore, R. G.; Eres, G.; Lee, H. N.; Du, M.-H.; Ward, T. Z.; Lee, J. S.; Weber, W. J.; Zhang, Y.; Brahlek, M. Adsorption-

- Controlled Growth of MnTe (Bi 2 Te 3) n by Molecular Beam Epitaxy Exhibiting Stoichiometry-Controlled Magnetism. *Phys. Rev. Mater.* 2020, 4 (11), No. 111201.
- (22) Trang, C. X.; Li, Q.; Yin, Y.; Hwang, J.; Akhgar, G.; Di Bernardo, I.; Grubišić-Čabo, A.; Tadich, A.; Fuhrer, M. S.; Mo, S.-K.; Medhekar, N. V.; Edmonds, M. T. Crossover from 2D Ferromagnetic Insulator to Wide Band Gap Quantum Anomalous Hall Insulator in Ultrathin MnBi ₂ Te ₄. ACS Nano 2021, 15 (8), 13444–13452.
- (23) Kagerer, P.; Fornari, C. I.; Buchberger, S.; Morelhão, S. L.; Vidal, R. C.; Tcakaev, A.; Zabolotnyy, V.; Weschke, E.; Hinkov, V.; Kamp, M.; Büchner, B.; Isaeva, A.; Bentmann, H.; Reinert, F. Molecular Beam Epitaxy of Antiferromagnetic (MnBi ₂ Te ₄)(Bi ₂ Te ₃) Thin Films on BaF ₂ (111). *J. Appl. Phys.* 2020, 128 (13), 135303. (24) Su, S.-H.; Chang, J.-T.; Chuang, P.-Y.; Tsai, M.-C.; Peng, Y.-W.; Lee, M. K.; Cheng, C.-M.; Huang, J.-C. A. Epitaxial Growth and Structural Characterizations of MnBi2Te4 Thin Films in Nanoscale. *Nanomaterials* 2021, 11 (12), 3322.
- (25) Chen, P.; Yao, Q.; Xu, J.; Sun, Q.; Grutter, A. J.; Quarterman, P.; Balakrishnan, P. P.; Kinane, C. J.; Caruana, A. J.; Langridge, S.; Li, A.; Achinuq, B.; Heppell, E.; Ji, Y.; Liu, S.; Cui, B.; Liu, J.; Huang, P.; Liu, Z.; Yu, G.; Xiu, F.; Hesjedal, T.; Zou, J.; Han, X.; Zhang, H.; Yang, Y.; Kou, X. Tailoring the Magnetic Exchange Interaction in MnBi2Te4 Superlattices via the Intercalation of Ferromagnetic Layers. *Nat. Electron.* 2022, 6 (1), 18–27.
- (26) Zhao, Y.-F.; Zhou, L.-J.; Wang, F.; Wang, G.; Song, T.; Ovchinnikov, D.; Yi, H.; Mei, R.; Wang, K.; Chan, M. H. W.; Liu, C.-X.; Xu, X.; Chang, C.-Z. Even—Odd Layer-Dependent Anomalous Hall Effect in Topological Magnet MnBi ₂ Te ₄ Thin Films. *Nano Lett.* 2021, 21 (18), 7691—7698.
- (27) Liang, Z.; Luo, A.; Shi, M.; Zhang, Q.; Nie, S.; Ying, J. J.; He, J.-F.; Wu, T.; Wang, Z.; Xu, G.; Wang, Z.; Chen, X.-H. Mapping Dirac Fermions in the Intrinsic Antiferromagnetic Topological Insulators (Mn Bi 2 Te 4) (Bi 2 Te 3) n (n = 0, 1). *Phys. Rev. B* 2020, 102 (16), No. 161115.
- (28) Wu, X.; Li, J.; Ma, X.-M.; Zhang, Y.; Liu, Y.; Zhou, C.-S.; Shao, J.; Wang, Q.; Hao, Y.-J.; Feng, Y.; Schwier, E. F.; Kumar, S.; Sun, H.; Liu, P.; Shimada, K.; Miyamoto, K.; Okuda, T.; Wang, K.; Xie, M.; Chen, C.; Liu, Q.; Liu, C.; Zhao, Y. Distinct Topological Surface States on the Two Terminations of MnBi 4 Te 7. *Phys. Rev. X* 2020, 10 (3), No. 031013.
- (29) Huang, Z.; Du, M.-H.; Yan, J.; Wu, W. Native Defects in Antiferromagnetic Topological Insulator MnBi 2 Te 4. *Phys. Rev. Mater.* 2020, 4 (12), No. 121202.
- (30) Du, M.-H.; Yan, J.; Cooper, V. R.; Eisenbach, M. Tuning Fermi Levels in Intrinsic Antiferromagnetic Topological Insulators MnBi2Te4 and MnBi4Te7 by Defect Engineering and Chemical Doping. Adv. Funct. Mater. 2021, 31 (3), No. 2006516.
- (31) Wang, G.; Zhu, X.; Sun, Y.; Li, Y.; Zhang, T.; Wen, J.; Chen, X.; He, K.; Wang, L.; Ma, X.; Jia, J.; Zhang, S. B.; Xue, Q. Topological Insulator Thin Films of Bi ₂ Te ₃ with Controlled Electronic Structure. *Adv. Mater.* 2011, 23 (26), 2929–2932.
- (32) Chen, Y. J.; Xu, L. X.; Li, J. H.; Li, Y. W.; Wang, H. Y.; Zhang, C. F.; Li, H.; Wu, Y.; Liang, A. J.; Chen, C.; Jung, S. W.; Cacho, C.; Mao, Y. H.; Liu, S.; Wang, M. X.; Guo, Y. F.; Xu, Y.; Liu, Z. K.; Yang, L. X.; Chen, Y. L. Topological Electronic Structure and Its Temperature Evolution in Antiferromagnetic Topological Insulator MnBi 2 Te 4. *Phys. Rev. X* 2019, 9 (4), No. 041040.
- (33) Hao, Y.-J.; Liu, P.; Feng, Y.; Ma, X.-M.; Schwier, E. F.; Arita, M.; Kumar, S.; Hu, C.; Lu, R.; Zeng, M.; Wang, Y.; Hao, Z.; Sun, H.-Y.; Zhang, K.; Mei, J.; Ni, N.; Wu, L.; Shimada, K.; Chen, C.; Liu, Q.; Liu, C. Gapless Surface Dirac Cone in Antiferromagnetic Topological Insulator MnBi 2 Te 4. *Phys. Rev. X* 2019, 9 (4), No. 041038.
- (34) Li, H.; Gao, S.-Y.; Duan, S.-F.; Xu, Y.-F.; Zhu, K.-J.; Tian, S.-J.; Gao, J.-C.; Fan, W.-H.; Rao, Z.-C.; Huang, J.-R.; Li, J.-J.; Yan, D.-Y.; Liu, Z.-T.; Liu, W.-L.; Huang, Y.-B.; Li, Y.-L.; Liu, Y.; Zhang, G.-B.; Zhang, P.; Kondo, T.; Shin, S.; Lei, H.-C.; Shi, Y.-G.; Zhang, W.-T.; Weng, H.-M.; Qian, T.; Ding, H. Dirac Surface States in Intrinsic Magnetic Topological Insulators EuSn 2 As 2 and MnBi 2 n Te 3 n + 1. Phys. Rev. X 2019, 9 (4), No. 041039.

- (35) Liu, M.; Lei, C.; Kim, H.; Li, Y.; Frammolino, L.; Yan, J.; Macdonald, A. H.; Shih, C.-K. Visualizing the Interplay of Dirac Mass Gap and Magnetism at Nanoscale in Intrinsic Magnetic Topological Insulators. *Proc. Natl. Acad. Sci. U. S. A.* 2022, 119 (42), No. e2207681119.
- (36) Hou, F.; Yao, Q.; Zhou, C.-S.; Ma, X.-M.; Han, M.; Hao, Y.-J.; Wu, X.; Zhang, Y.; Sun, H.; Liu, C.; Zhao, Y.; Liu, Q.; Lin, J. Te-Vacancy-Induced Surface Collapse and Reconstruction in Antiferromagnetic Topological Insulator MnBi2Te4. *ACS Nano* 2020, *14* (9), 11262–11272.